C.R.

IN-35867

# F I N A L  R E P O R T

NASA GRANT NAGW-444

## Basalt depths in lunar basins using impact craters as stratigraphic probes: Evaluation of a method using orbital geochemical data

by

Constance G. Andre (P.I.)
Center for Earth and Planetary Studies
Smithsonian Institution

October 1986

## ABSTRACT

A rare look at the chemical composition of subsurface stratigraphy in lunar basins filled with mare basalt is possible at fresh impact craters. Mg/Al maps from orbital X-ray flourescence measurements of mare areas indicate chemical anomalies associated with materials ejected by large post-mare impacts. The objective of this research is to evaluate a method of constraining the wide-ranging estimates of mare basalt depths using the orbital Mg/Al data and compare the results to those of investigators using different indirect methods.

Chemical anomalies at impact craters within the maria indicate five locations where higher Mg/Al basalt compositions may have been excavated from beneath the surface layer. At eight other locations, low Mg/Al anomalies suggest that basin-floor material was ejected. In these two cases, the stratigraphic layers are interpreted to occur at depths less than the calculated maximum depth of excavation. In five other cases, there is no apparent chemical change between the crater and the surrounding mare surface. This suggests homogeneous basalt compositions that extend down to the depths sampled, i.e., no anorthositic material that might represent the basin floor was exposed.

The limitations on basalt thickness inferred from the orbital XRF data are largely consistent with basalt isopach maps based on measurements of the exposed rim heights of partially buried craters in mare filled basins.

Interpretations of these Mg/Al data at several impact craters in Mare Serenitatis are compared to stratigraphic models proposed by other investigators.

# INTRODUCTION

Since the Apollo missions to the Moon, estimates of mare basalt depths in lunar basins have become progressively smaller, from tens of kilometers to tenths of kilometers. The indirect methods used in the past to determine the thickness of volcanic deposits and corresponding volume estimates of lavas extruded onto the lunar surface are: (1) interpretation of seismic and gravity data (Toksoz et al., 1972; Thurber and Solomon, 1985); (2) topographic studies of unfilled basin morphometry (Head, 1976); (3) stratigraphic relationships relative to mare surfaces (Head, 1981); (4) the extent to which basalts have buried the rims of premare craters (Dellon and Waskom, 1976; Dellon, 1979); (5) the redefinition of assumptions of the method used by Dellon and Wascom (1976) to predict lower calculated basalt depths (Horz, 1978) and (6) the reinterpretation of seismic data (Goins et al., 1981).

The limitations of each of these indirect methods makes it necessary to combine results and seek new ways to evaluate them. Orbital X-ray fluorescence (XRF) data at fresh impact craters in a few specific locations in the maria provide still another means for constraining the wide range of estimates. From basalt depth information, there is a better understanding of basalt volumes, basin configurations, impact processes and constraints on gravity and seismic interpretations.

Eratosthenian and Copernican impact craters in mare areas can be used as stratigraphic probes when they can be detected as anomalies in orbital X-ray fluorescence (XRF) data. Mg/Al ratios calculated for surface soils at craters that are within the resolution of the XRF detectors are compared to the Mg/Al average of the surrounding mare surface. Low Mg/Al ratios associated with post-mare impacts would indicate that more anorthositic material from beneath

the basalt fill had been exposed; whereas significantly higher Mg/Al ratios would suggest that a basalt layer of a different chemical composition had been sampled. Preimpact and postimpact positions of materials from various depths from laboratory cratering experiments, natural terrestrial analogs, chemical and nuclear tests and theoretical studies are used to constrain depths to crustal material beneath mare basalts.

The fundamental premise of the orbital XRF data interpretation is that basalt fill in the basins (high Mg/Al material) is generally lense-shaped and that the anorthositic composition of the highlands (low Mg/Al material) surrounding the maria is comparable to the basin floor underlying it. This premise is supported by crustal thickness maps based on the Airy compensation model (Bills and Ferrari, 1976), by the shallow (1:10) depth/diameter ratio estimated for basin excavations (Croft, 1981) and by the anorthositic nature of basin ejecta (Spudis, 1983 and Andre, 1981).

## METHODS AND LIMITATIONS

The objective of this orbital XRF study is primarily to develop a technique, not to place well-defined limits on the depth of basalt accumulations in lunar basins. Many potentially useful shallow craters were omitted because of spatial resolution constraints, statistical errors and nonchemical interorbit variations in the data. Despite these draw-backs, the results of the survey are encouraging for future high-resolution XRF remote sensing to refine knowledge of mare stratigraphy.

Mg/Al ratios from irregularly-spaced points within the overlapping coverage of the Apollo 15 and 16 overflights were combined into a digital map of $7.5^2$ km elements. The values for data points occurring within the XRF field-of-view (FOV) were resampled with sliding boxcar filters, weighted to simulate the varying signal intensity of the detector. For a more detailed description of corrections made to the data and processing procedures, see Bielefeld et al. (1977).

For the purpose of this study, the Mg/Al ratio is preferable to either the Al/Si or Mg/Si ratio because it is the only one that can be used to distinguish KREEP and Low-K Fra Mauro basalts from anorthositic terra compositions. All three compositions can have the same Al/Si and Mg/Si concentrations; whereas the Mg/Al concentrations for anorthosite, gabbroic anorthosite and anorthositic gabbro are consistently below that for KREEP and Low-K Fra Mauro basalts that rarely fall below 0.4. Mg/Al concentrations for rock and soil samples returned from the moon are compared to a frequency diagram of orbital XRF Mg/Al intensity ratios, equivalent calculated Mg/Al concentration ratios and corresponding density numbers (DN) of the Mg/Al digital image (Fig. 1).

Spatial resolution considerations:

How small an impact crater could create a chemical anomaly on the mare surface that could be detected in the orbital XRF data? Five things must be considered: (1) the size of the feature relative to the orbital XRF field-of-view (FOV); (2) the varying response of the XRF detector; (3) the percent difference between the Mg/Al ratio for crater materials and for the surrounding mare surface; (4) the signal to noise level of the XRF instrument; and (5) the radial extent to which material from the subsurface layer blankets the area. A graph was constructed to show the relationships among these factors (Fig. 2) The following assumptions were made: (1) the anomaly is circular and chemically homogeneous; and (2) the surrounding mare terrain is chemically homogeneous and fills the remainder of the FOV.

The "% difference in the elemental ratio at the lunar surface" is calculated from a series of ratio pairs assigned to an anomaly and to the surrounding area. Chemical anomalies with radii of 5 km, 10 km, 15 km, 30 km and 60 km were considered. In each case, a corresponding % difference that would be detected by the orbiting XRF spectrometer was calculated. A feature of 60 km radius would account for 100% of the secondary x-ray signal when centered within the FOV; therefore, the contrast measured by the XRF detector would accurately reflect the contrast in lunar surface soils, as shown on the graph. For anomalies smaller than that, however, the contrast measured from orbit will decrease (due to artificial mixing of the X-ray signal from the two areas) according to the response function of the XRF instrument. The detector is most efficient at the subsatellite point, such that 50% of the signal is from a central area in the FOV that is about 10 km in radius.

The graph (Fig. 2) indicates that the smallest detectable anomaly in the

orbital XRF data would be 5 km in radius, only if the ratio difference between the chemical feature and the surrounding mare were at least 150%. For instance, if a chemical anomaly 5 km in radius has an Mg/Al concentration of 0.2 (e.g., gabbroic aorthosite) compared to surrounding basalts with an Mg/Al concentration of 0.8, the difference is 0.6. This difference represents a 300% increase over the chemical anomaly. However, in the orbital XRF data the difference between the anomaly and the surrounding basalts would appear to be no more than 10%, just above the critical signal/noise level. Below that point, a chemical variation could not be detected.

Cratering mechanics:

The smallest detectable anomaly in the orbital XRF data can be defined in terms of the smallest potentially useful crater for this study, according to models of crater mechanics.

The sequence of events during an impact and the mechanical rearrangement of pre-target materials are important to the interpretation of stratigraphy from orbital chemical data. Theoretical calculations of impact processes Maxwell, 1977; Croft, 1980), laboratory studies of impact craters (Stoffler et al., 1975) and investigations of natural and explosion impact craters on Earth (Shoemaker, 1960; Gault, 1974; Jones, 1977; Roddy, 1973, 1977; Moore, 1977) confirm that the deepest materials excavated range beyond the rim crest and are positioned on top of ejecta from shallower levels of excavation. When applied to the lunar case, this means that subsurface material in a crater too small to be resolved with the XRF detector could be distinguished because of the lateral extension provided by the ejecta.

The inverted order of preimpact stratigraphy can be seen at Meteor Crater in Arizona and at Middle Gust and Mixed Company explosion craters (Roddy, 1973). Material from the deepest levels of excavation appear on top, closest to the crater rim. The final positions of successively shallow strata are at lower levels of continuous ejecta deposits and are visible on the surface only at increasing distances from the crater. The deepest and last material excavated is not ejected beyond the creater rim, but falls back into the crater and settles on top of the breccia lens (Roddy, 1977).

Many studies of continuous deposits around terrestrial impact craters can't be applied directly to geochemical studies of crater deposits on planets using remote sensing data. For instance, a detailed study of the Ries crater in Germany (Horz et al., 1983) was limited to weight % calculations of pre-impact strata from cores drilled at various radial distances from the crater through

the entire thickness of the continuous deposit. Thus, the proportions of the crater deposits attributed to specific layers of the target zone are volumetric measurements and bear little relation to the surficial view from an orbiting spectrometer. In fact, two Ries clasts alone account for about 45% of the weight of all crater materials observed in the drilling project. The authors conclude that the Ries crater continuous deposits exhibit only a crude approximation of inverted stratigraphy and that deep-seated material from the target is a minor component in the ejecta beyond the tectonic rim. However, from the remote sensing perspective, these results are seriously skewed. A more appropriate way to describe the source of terrestrial impact deposits as an analog to planetary impact crater ejecta as viewed from orbit by spectral reflectance and XRF instruments that measure less than the top 20 um of the surface, would be the proportion of deep target to shallow target ejecta in surface samples collected at increasing radial distances from the center of the crater. If the crater is not extensively eroded, it is expected that the inverted stratigraphy and existence of deep crater ejecta on the surface at and beyond the rim crest would be statistically significant. If such measurements were possible at the Ries crater, the results would be more likely to reflect the ejecta stratification findings predicted by cratering mechanics theory, observed in explosion craters and laboratory impact tests, as well as geochemical data (Andre et al., 1979), spectral reflectivity data (Pieters, 1977) and by astronaut observations (El-Baz and Worden, 1972) of the Moon.

Hypervelocity impact experiments (Stoffler et al, 1975) were conducted to trace the final positions of colored sand ejecta from horizontal reference strata. Material displaced from the upper 15% of the crater depth, d (rim to bottom), is represented within the whole ejecta blanket that extends more than 6.5 crater radii from the center of impact. Material from deeper than 28% of d is deposited inside 2 crater radii and no material from deeper than 33% of d was

ejected beyond the crater rim. It has an inverted order of stratigraphy relative to the original target strata.

If an impact crater 10 km wide and 2 km deep formed in a two-layer target, in which low Mg/Al anorthositic material lies below high Mg/Al mare surface only a few meters thick, anorthositic ejecta could extend to 7 crater radii from the center of impact (Stoffler et al., 1975). However, beyond the continuous ejecta deposit, the two compositions are mixed by secondary impacts (Oberbeck, 1975). Thus, the clearest evidence for excavation of subsurface material of a different composition that might appear in the orbital XRF data lies in the continuous deposits. Moore (1974) defined the relationship between crater radius ($R_c$) and continuous ejecta radius ($R_{ce}$) as:

$$R_{ce} = 2.348\ R_c^{\ 1.006}$$

If the minimum radius of an anomaly (continuous ejecta) with Mg/Al concentrations 150% lower than the surrounding mare that could be detected in the orbital XRF data is 5 km, the corresponding crater radius would be 2.1 km. The smallest impact crater included in this survey has a radius of 2.5 and a calculated continuous ejecta blanket 5.9 km in radius .

Criteria for craters used in the survey:

1) The crater was formed by impact into a mare area of the Moon.

2) The crater is of Eratosthenian or Copernican age (post-mare).

3) the crater at least 5 km in diameter with a calculated continuous ejecta blanket 11.8 in diameter.

4) At least one orbital XRF data collection point lies within the continuous ejecta of the crater.

5) The edge of the continuous ejecta is more than 10 km from the nearest mare/terra contact.

6) The crater interior has not been flooded with mare basalts.

Thirty-two craters met the criteria listed above. Information was tabulated on the crater ages, the 1:250,000 Lunar Topographic Orthophoto Map (LTO) where they can be found, the rim crest radius, the calculated extent of the continuous ejecta, the number of orbital XRF data points inside the area of continuous ejecta, and the depth of the crater from rim to floor (Table 1).

The Mg/Al digital map was used to evaluate chemical changes at these craters because by combining neighboring data points within the FOV, counting statistics are improved. Spatial resolution limitations restrict the study to relative rather than absolute Mg/Al concentration differences between crater material, representing the subsurface composition and the surface composition of the adjacent mare. Thus, no effort was made to convert density numbers (DN) from the map to Mg/Al concentrations. The area within the crater rim, the area between the rim and the boundary of the continuous ejecta, and beyond that, a mare area with a radial distance the same as the continuous ejecta were plotted on the digital Mg/Al map. The mean Mg/Al density number and standard deviations for each area were determined.

Three other calculations are needed to evaluate the Mg/Al means for each concentric crater area: the estimated depth of excavation from which ejecta beyond the rim is derived (Stoffler et al., 1975), the difference in DN between the crater and the mare beyond the continuous ejecta and the overlap between their standard deviations to omit any greater than DN = 5 (Table 2).

The final step is to interpret the high or low Mg/Al anomalies with standard deviation overlaps less than 5 DN in terms of whether the total accumulation of basalts are greater than (GT) or less than (LT) the estimated depth of excavation for that crater. Unless the average DN for the crater represents a decrease or increase of 3 relative to the mare average, the chemical composition for the crater materials and surrounding mare surface are considered homogeneous from the orbital XRF perspective. That is, there is no evidence that the

deepest material sampled is different from the mare surface basalts. A mean crater DN higher than the mare value by 3 or more, suggestes that the total accumulation of basalts in this area may exceed the maximum excavation depth of the crater. In fact, it suggests excavation of an earlier basalt flow with a richer concentration of Mg/Al than those on the surface. On the other hand, A DN decrease of 3 or more for the crater relative to the mare implies that the basin floor contact may lie at depths less than the calculated excavation depth.

The results of the orbital XRF survey are then compared to the results of two different basalt thickness interpretations of measurements of exposed rim heights of partially buried craters in the mare (DeHon and Waskom, 1976; Horz, 1978). The location of the craters are plotted on an isopach map of mare basalts calculated by an independent method (DeHon and Waskom, 1976).

## RESULTS

Results of the orbital XRF impact crater survey are shown in Table 2. Interpretations were possible for eighteen craters screened from the original thirty-two for higher statistical certainty. Maximum and minimum depths to the base of mare basalt accumulations in the basins were estimated for each crater using Mg/Al data and calculated levels from which the deepest crater ejecta near the rim is derived.

Of the eighteen craters, five are associated with increased Mg/Al concentrations relative to the mare surface (from a subsurface basalt horizon of a different chemical composition?); eight have decreased Mg/Al concentrations (sampled from the basin floor beneath the mare fill?); and five have no apparent change (no evidence of increased anorthositic component?).

Fifteen of the craters in the orbital XRF survey are in areas where basalt depth constraints can be compared to basalt isoach maps from investigators using other techniques: 1) those by Dellon and Waskom (1976) and Dellon (1979) who base their estimates of maximum basalt depths on fresh crater morphometry and 2) those by Horz (1978) who reduces those estimates by half to account for the degradation of pre-mare craters to the extent of a randomly sampled population of craters in the highlands. In 12 of the 15 cases, the Mg/Al data constraints on basalt depths agreeed with those of Dellon (1979) and Dellon and Waskom (1976). In 10 of the 15 cases, the orbital Mg/Al data agreed with estimates of Horz (1978).

In the next section, both high and low Mg/Al anomalies at impact craters in Mare Serenitatis will be discussed to demonstrate how the orbital XRF data can be used to detect irregularities in basin configuration and constrain the depths of basalts that fill them.

## DISCUSSION

Mg/Al data at impact craters in Mare Serenitais add a new stratigraphic dimension to a variety of remote sensing studies of the area. Bessel crater in central Mare Serenitatis has an average Mg/Al concentration 2.0 lower than the surrounding mare surface. The chemical contrast implies that anorthositic material beneath the mare basalts has been exposed. Young (1977) observed a thin dark layer about 500 m below the crater rim on Apollo 15 and 17 panoramic camera frames. He proposed that it is an extension of the dark mantle annulus of southern Mare Serenitatis that dips less than 0.15 degrees under younger lavas of the interior basin. Considering the morphometry of Bessel and the mechanics of impact cratering, could the impact have distributed low Mg/Al material from below the dark layer at a sufficiently wide range to be detected by the orbiting XRF spectrometer?

Bessel is 1700 m deep measured from crest to floor (d) and has been excavated to a depth of 560 m (Table 2). The dark layer at 500 m below the rim is 29% of d. Material from about 28% of d is deposited at a range of 2 crater radii from the center of impact (Stoffler et al, 1975). Thus, if anorthositic basin floor material lies immediately below the dark layer in Bessel, homogeneous to the deepest levels of excavation, it would create a blanket of ejecta 15.4 km in diameter. This calculation is a minimum estimate based on cratering experiments into quartz sand; a wider dispersion of ejecta would be expected for impacts into hard rock (Stoffler et al., 1975).

Meteorite impacts between the time of basin formation and the episodes of volcanism that filled them created an irregular basin floor. Bessel appears to have formed on an arch (Scott et al., 1978) that is part of a circular mare ridge system 140 km in diameter. It implies that an impact structure buried beneath the mare surface (Maxwell et al., 1975), that could have been almost 5 km deep when it formed (Croft, 1978). If this is so, the depths of basalts on

either side of this ridge system should increase. In fact, ridges often mark the transition between thick and thin basalts and are seldom found in regions of uniform basalt thickness (Dellon and Waskom, 1976).

If Bessel (#6, Fig. 3) impacted a topographic high of the premare basin, anorthositic materials would lie closer to the mare surface there where they could be exposed in the ejecta and fallback of the crater. If this is the correct explanation for the low Mg/Al concentrations associated with Bessel, the level of the basin floor would fall off sharply from the buried rim and basalt accumulations would be correspondingly thicker. Although Bobillier less than 125 km SE of Bessel and Borel, less than 250 km NE of Bessel, are small craters, Mg/Al concentrations associated with them exceed the mean values for the adjacent mare and in both cases the standard deviations for crater vs mare material do not overlap. The higher Mg/Al ratios at Bobillier relative to the surrounding basalt surface suggest that the more recent lava that flooded outside the rim of the crater (Young, 1977) have lower concentrations of Mg/Al than the subsurface basalts exposed at the crater. The subsurface layer sampled by these impacts at levels of 430 m and 330 m, respectively, may be part of the dark layer in the wall of Bessel crater (and the dark border units that Young (1977) proposed is a basin-wide dark mantle layer. Orbital XRF data indicates that dark mantle exposed along border units in southern and eastern Mare Serenitatis is magnesium rich. High magnesium basalts are also seen as peripheral units of Mare Crisium and Mare Fecunditatis and associated with impact craters in the centers of these maria (Andre et al., 1978, 1979). The high-Mg material detected in the orbital XRF data suggests that the earliest stages of volcanism in those basins are part of basin-wide layers, largely buried by younger less-magnesian flows, except along discontinuous mare benches at the basin edge.

The averaged Mg/Al values for Tacquet (#26, Fig. 3) and Sulpicious Gallus (#24, Fig. 3), are lower than the dark mantle annulus of Serenitatis where they

are located. If these differences are real, submare material may be exposed at Tacquet and Sulpicious Callus at depths less than 430 m and 695 m, respectively. These estimates are consistent with the estimates of Dellon and Waskom (1976).

Acknowledgments: My thanks to Rose Aiello for her drafting help.

REFERENCES:

Andre, C. G. (1981) Chemcal rings of lunar basins from orbital X-ray data. In: Multi-ring Basins, Proc. Lunar Planet. Sci. Conf. 12A, p. 125-132. Ed. P. H. Schulz and R. B. Merrill.

Andre C.G. and Adler I. (1978) Edidence for a high-magnesium subsurface basalt in Mare Crisium from orbital X-ray fluorescence data. In: Mare Crisium: The View from Luna 24 (R.B. Merrill and J. J. Papike, eds.), p. 1-12. Pergamon, N.Y.

Andre C. G., Wolfe R. W. and Adler I. (1979) Are early magnesium-rich basalts widespread on the Moon? Proc. Lunar Planet. Sci. Conf. 10th, p. 1739-1751.

Bielefeld, M.J., Andre, C.G., Eliason, E.M., Clark, P.E., Adler I., and Trombka, J.I. (1977) Imaging of lunar surface chemistry from orbital X-ray data. Proc. Lunar Sci Conf 8th, p. 901-908.

Bills, B. G. and Ferrari, A. J. (1976) Lunar crustal thickness. Proc. Lunar Sci. Conf. 7th, frontispiece.

Croft S.K. (1978) Lunar crater volumes: Interpretation by models of impact cratering and upper crustal structure. Proc. Lunar Planet. Sci. Conf. 9th, p. 3711-3733 .

Croft, S.K. (1980) Cratering flow fields: Implications for the excavation and transient expansion stages of crater formation. Proc. Lunar Planet. Sci. Conf. 11th, p. 2347-2378.

Croft, S. K. (1981) The excavation stage of basin formation: A qualitative model. In: Multi-ring Basins, Proc. Lunar Planet. Sci. 12A, (P.H. Schulz and R. B. Merrill, eds.), p. 207-225.

De Hon R. A. (1979) Thickness of the western mare basalts. Proc. Lunar Planet. Sci. Conf. 10th, p. 2935-2955.

De Hon R. A. and Waskom J. D. (1976) Geologic structure of the eastern mare basins. Proc. Lunar Sci. Conf. 7th, p. 2729-2746.

El-Baz F. and Worden A. M. (1972) Visual observations from lunar orbit. In Apollo 15 Preliminary Science Report, NASA SP-289, p. 25-1 to 25-27.

Gault, D. (1974) Impact Cratering. In: A Primer in Lunar Geology (R. Greeley and P. Schultz, eds.), p. 137-175. NASA TM 62,359.

Goins N.R., Dainty A.M. and Toksoz M.N. (1981) Structure of the lunar crust at highland site Apollo Station 16, GRL, vol. 8, no 1, p. 29-32.

Head, J. W. (1976) Lunar volcanism in space and time. Rev. Geophys. and Space Phs. vol. 14, no. 2, p. 265-300.

Head J. W. (1981) Lava flooding of ancient planetary crusts: Geometry, thickness, and volume of flooded lunar impact basins. Moon and Planets, vol. 26, p. 61-88.

Horz F. (1978) How thick are lunar mare basalts? Proc. Lunar Planet. Sci. Conf. 9th, p. 3311-3332.

Horz F., Ostertag R. and Rainey D. A. (1983) Bunte Breccia of the Ries: Continuous deposits of large impact craters. Rev. Phys. and Space Phys., vol. 21, no. 8, p. 1667-1725.

Jones C.H.S. (1977) Complex craters in alluvium. Impact and Explosion Cratering (D. J. Roddy, R. O. Pepin and R. B. Merrill, eds.) Pergamon Press, N.Y., p. 163-183.

Maxwell, T. A., El-Baz, F. and Ward, S. H. (1975) Distribution, morphology, and origin of ridges and arches in Mare Serenitatis. GSA Bulletin, V. 86, p. 1273-1278.

Maxwell, D. E. (1977) Simple Z model of cratering, ejection, and overturned flap. In Impact and Explosion Cratering (D. J. Roddy, R. O. Pepin and R. B. Merrill, eds.) Pergamon Press, N.Y., p. 1003-1008.

Moore H J. (1977) Nevada test site craters used for astronaut training. JGR v. 5, n. 6, p. 719-733.

Moore H. J., Hodges C.A. and Scott D. H. (1974) Multiringed basins--Illustrated by Orientale and associated features. Proc. Lunar Sci. Conf. 5th, p. 71-100.

Oberbeck, V. R. (1975) The role of ballistic erosion and sedimentation in lunar stratigraphy. Rev. Geophys. and Space. Phys., p. 337-362.

Pieters, C. (1977) Characterization of lunar basalt types--II: Spectral classification of fresh mare craters. Proc. Lunar Sci. Conf. 8th, p. 1037-1048.

Roddy, D. J. (1973) Project LN 303, geologic studies of the Middle Gust and Mixed Company: Mixed Company/Middle Gust Results Mtg. 3-15 March 1973, Defense Nuclear Agency DNA 3151 P2, unclassified, p. 79-123.

Roddy, D. J. (1977) Large-scale impact and explosion craters: comparisons of morphological and structural analogs. Impact and Explosion Cratering, Pergamon Press, N.Y., p. 185-246.

Scott, D. H., Watkins, J. S. and Diaz, J. M. (1978) Regional deformation of mare surfaces. Proc. Lunar Planet. Sci. Conf. 9th, p. 3527-3539.

Shoemaker, E. (1960) Penetration mechanics of high-velocity meteorites illustrated by Meteor Crater, Arizona. International Geological Congress, 21st session, Part XVII, p. 418-434.

Spudis, P. D. (1983) The excavation of lunar multi-ring basins: Additional results for four nearside basins. In: Lunar and Planetary Science XIV, p. 735-736

Stoffler, D., Gault, D. E., Wedekind, J. and Polkowski, G. (1975) Experimental hypervelocity impact into quartz sand: distribution and shock metamorphism of ejecta. JGR, v. 89, n. 29, p. 4062-4077.

Thurber C. H. and Solomon S. C. (1978) An assessment of crustal thickness variations on the lunar near side: models, uncertainties, and implications for crustal differentiation, Proc. Lunar and Planet Sci. Conf. 9th, p. 3431-3497.

Toksoz M.N., Press F., Anderson K., Dainty A., Latham G., Ewing M., Dorman J., Lamlein G., Sutton F., Duennebier F. and Nakamura Y. (1972) Lunar crust: structure and composition, Science, 176, p. 1012-1016.

Young, R. A. (1977) A stratigraphic model for Bessel Crater and southern Mare Serenitatis. Impact and Explosion Cratering. Pergamon Press (New York), p. 527-538.

FIGURE AND TABLE CAPTIONS

Fig. 1. Mg/Al concentrations of lunar rocks and soils are compared to a frequency distribution of the orbital XRF Mg/Al intensity ratios, calculated concentration ratios and density numbers (DN) on an Mg/Al digital map of the corrected and processed data (Bielefeld, 1977).

Fig. 2. The graph shows the degree to which the orbital XRF measurement of a chemical anomaly smaller than the FOV is degraded as a function of its size and chemical contrast to the surrounding area.

Fig. 3. Post-mare craters used in this study are plotted on an isopach map of mare basalts using an independent method described in the text (Dellon and Waskom, 1976). Numbers refer to craters listed in Table 2. See Table 2 for a comparison of results.

Table 1. Lunar post-mare impact craters in nearside basins that meet the criteria for this study.

Table 2. Impact crater calculations.

Fig. 1

# Mg/Al CONCENTRATION IN SAMPLES VS ORBITAL VALUES

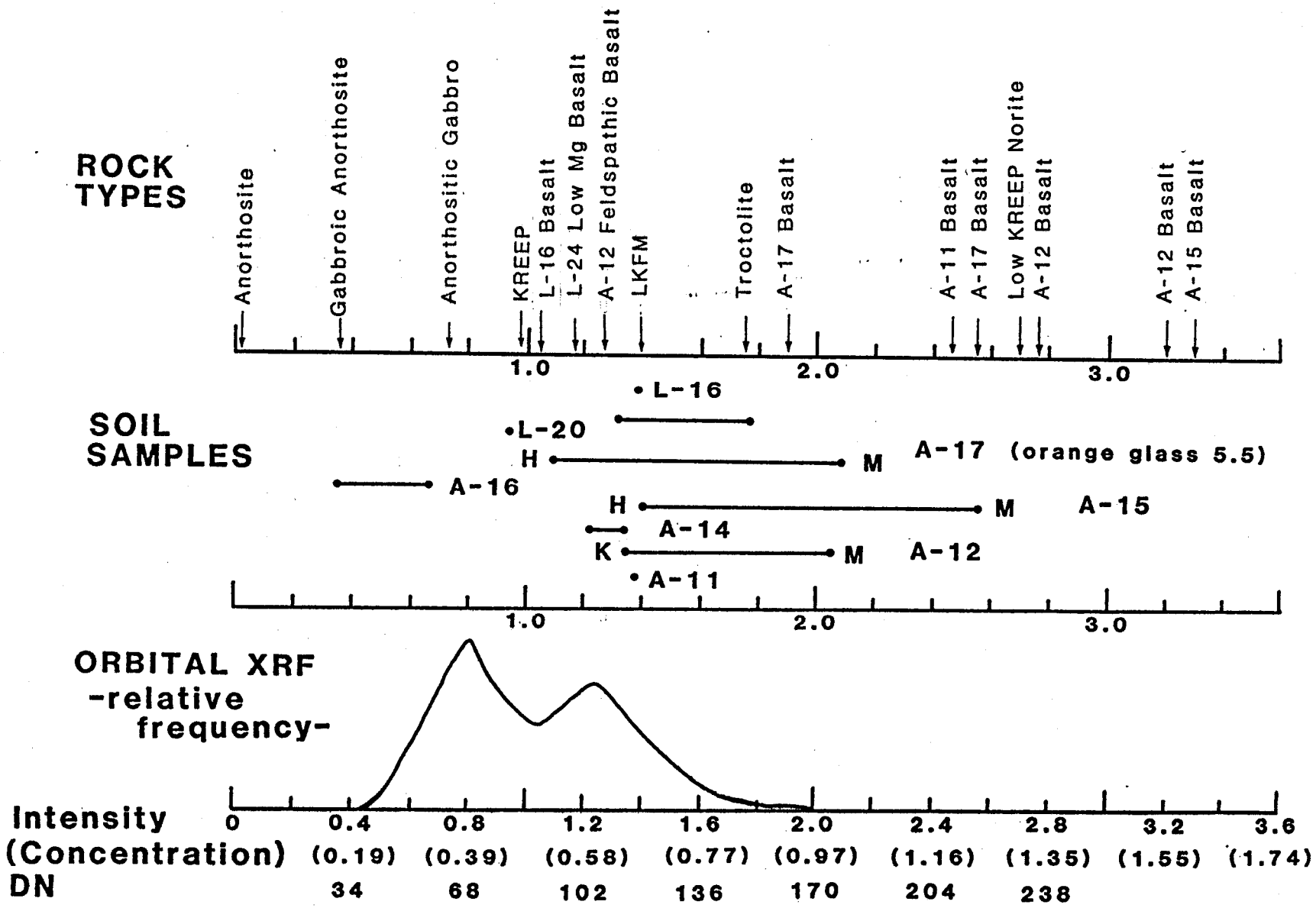

Fig. 2

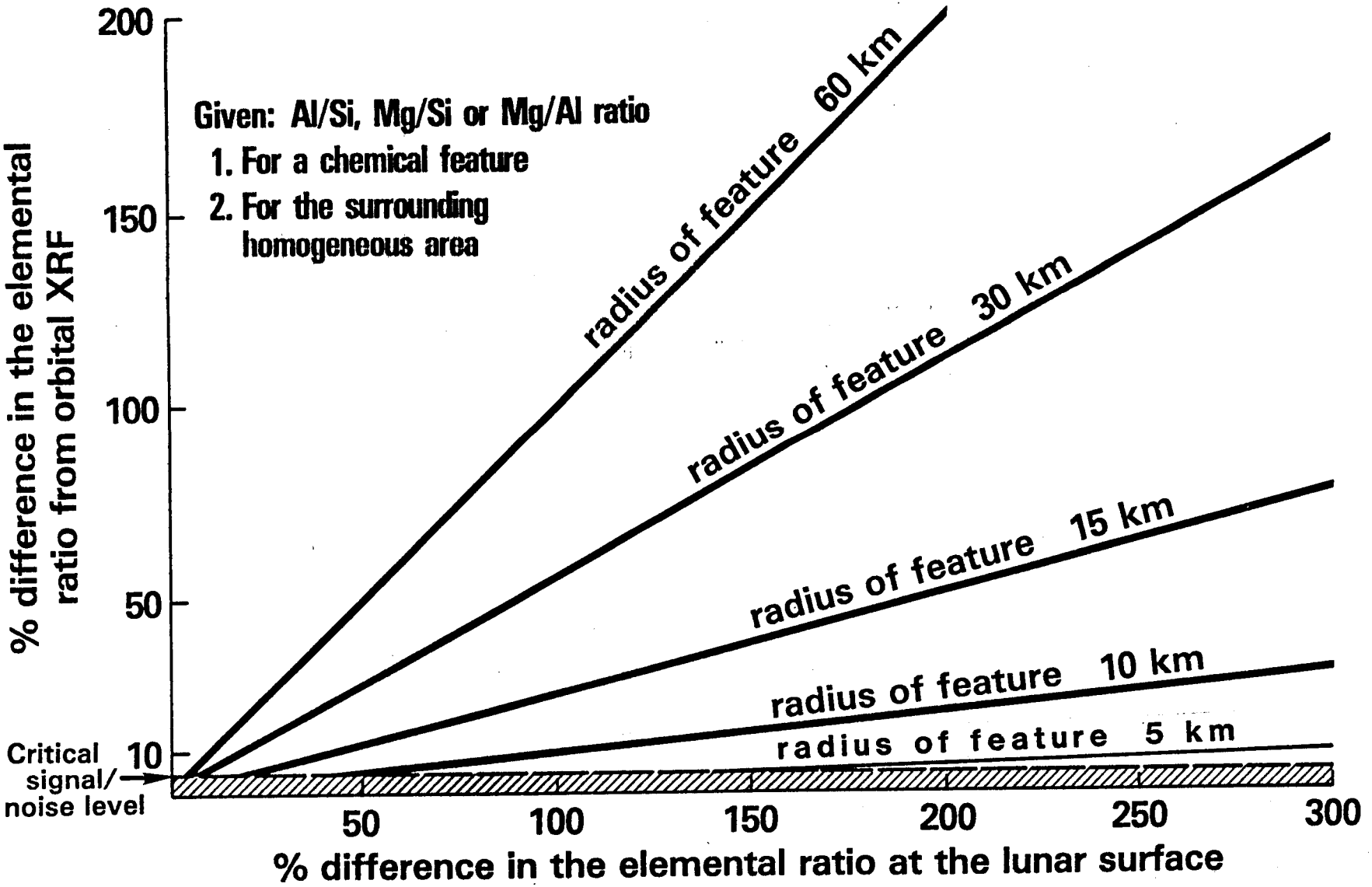
200
150
100
50
10
Critical signal/noise level
% difference in the elemental ratio from orbital XRF
Given: Al/Si, Mg/Si or Mg/Al ratio
1. For a chemical feature
2. For the surrounding homogeneous area
radius of feature 60 km
radius of feature 30 km
radius of feature 15 km
radius of feature 10 km
radius of feature 5 km
50
100
150
200
250
300
% difference in the elemental ratio at the lunar surface

Fig. 3

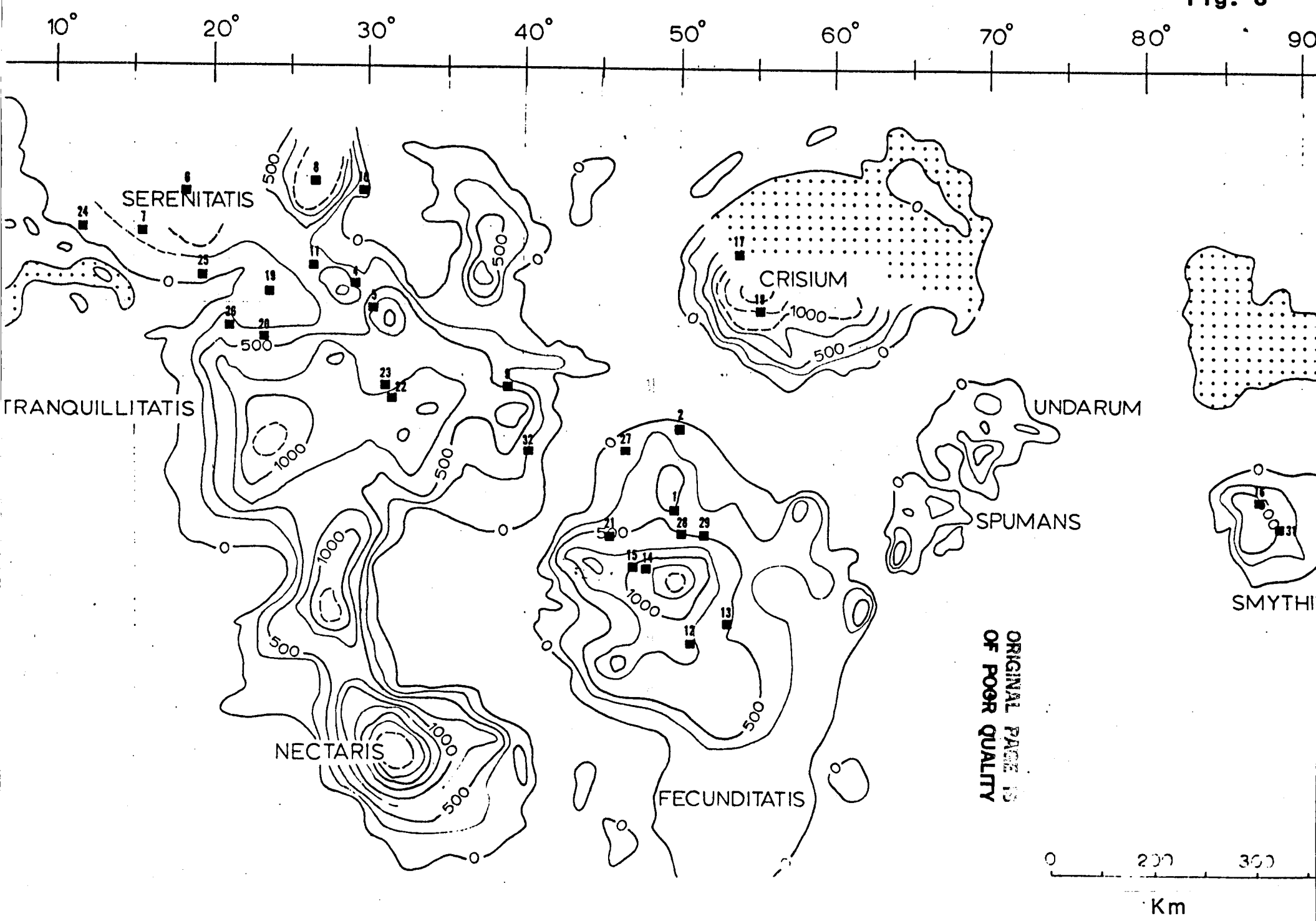

Table 1. Impact craters that meet the criteria for this study:

| Crater | Age | LTO* | Long/Lat | R (km) | $R_{ce}$ (km) | XRF pts in CE | d (km) |
|---|---|---|---|---|---|---|---|
| Anville (Taruntius G) | E | 61C3 | 49°30'E; 1°50'N | 4.8 | 11.3 | 2 | 2.1 |
| Asada (Taruntius A) | E | 61C2 | 49°55'E; 7°15'N | 6.1 | 14.4 | 2 | 2.6 |
| Beer | C | 41A4 | 9°5'W; 27°5'N | 4.8 | 11.3 | 2 | 1.5 |
| Beketov (Jansen C) | E | 42C3 | 29°10'E; 16°15'N | 3.5 | 8.3 | 1 | 1.0 |
| Bernini (Jansen L) | E | 61A1 | 30°5'E; 14°40'N | 3.5 | 8.3 | 1 | 1.4 |
| Bessel | E | 42D2 | 17°55'E; 21°40'N | 7.7 | 18.3 | 1 | 1.7 |
| Bobillier (Bessel E) | E | 42D3 | 15°25'E; 19°35'N | 3.0 | 7.1 | 1 | 1.3 |
| Borel (Le Monnier C) | E | 42C2 | 26°25'E; 22°20'N | 2.8 | 6.6 | 1 | 1.0 |
| Cauchy | C | 61A3 | 38°35'E; 9°35'N | 6.4 | 15.2 | 2 | 2.6 |
| Clerke (Littrow B) | C | 42C2 | 29°45'E; 21°40'N | 3.0 | 7.3 | 1 | 1.3 |
| Dawes | E | 42C3 | 26°20'E; 17°10'N | 8.2 | 19.5 | 7 | 2.4 |
| Ibn Battuta (Goclenius A) | E | 80A4 | 50°25'E; 7°S | 5.8 | 13.7 | 4 | 1.2 |
| Lindbergh (Messier G) | E | 80A4 | 52°50'E; 5°25'S | 7.5 | 17.9 | 11 | 1.8 |

(continued on next page)

| Crater | Age | LTO | Long; Lat | R (km) | $R_{ce}$ (km) | XRF pts. in CE | d (km) |
|---|---|---|---|---|---|---|---|
| Messier | C | 79B2 | 47°35'E; 1°55'S | 4.1 | 9.8 | 5 | 1.9 |
| Messier A | C | 79B2 | 46°55'E; 2°5'S | 5.3 | 17.6 | 3 | 2.2 |
| Peek | C | 63C3 | 86°55'E; 2°45'N | 6.3 | 14.9 | 12 | 2.3 |
| Peirce | E | 44D4 | 53°20'E; 18°15'N | 9.4 | 22.4 | 3 | 2.1 |
| Picard | E | 62A1 | 54°45'E; 14°30'N | 11.2 | 26.7 | 6 | 2.2 |
| Plinius | E | 60B1 | 23°35'E; 15°20'N | 17.2 | 41.3 | 24 | 3.0 |
| Ross | E | 60B4 | 21°45'E; 11°40'N | 13.0 | 31.2 | 2 | 2.2 |
| Secchi K | E | 79B2 | 45°30'E; 0°10'S | 3.4 | 8.0 | 1 | 1.3 |
| Sinas | E | 61A4 | 31°35'E; 8°50'N | 6.5 | 15.5 | 2 | 2.2 |
| Sinas E | E | 61A4 | 31°E; 9°40'N | 5.3 | 12.5 | 1 | 1.9 |
| Sulpicious Gallus | C | 42D4 | 11°40'E; 19°40'N | 5.5 | 12.1 | 2 | 2.1 |
| Tacquet | E | 42D3 | 19°10'E; 16°35'N | 3.3 | 7.8 | 1 | 1.3 |
| Tacquet C | E | 60B1 | 21°5'E; 13°30'N | 2.9 | 6.8 | 1 | 1.8 |
| Taruntius | C | 61C2 | 46°30'E; 5°30'N | 28.0 | 67.0 | 59 | 1.2 |
| Taruntius H | C | 61C3 | 49°50'E; 0°20'N | 4.2 | 9.9 | 2 | 1.8 |
| Taruntius P | E | 62D4 | 51°35'E; 0°5'N | 3.4 | 8.0 | 1 | 1.4 |
| Timocharis | C | 40B3 | 13°10'W; 26°40'N | 16.5 | 39.6 | 17 | 2.8 |
| Unnamed in Smythii | E? | 63C3 | 88°20'E; 1°15'N | 2.5 | 5.9 | 3 | 0.7 |
| Zahringer (Taruntius E) | E | 61C1 | 40°10'E; 5°30'N | 5.3 | 12.5 | 6 | 2.2 |

*Lunar Topographic Orthophotomaps, 1:250,000

C = Copernican
E = Eratosthenian
R = rim crest radius
$R_{ce}$ = calculated radius of continuous ejecta (Moore et al., 1974)
d = rim to floor depth

Table 2. Impact crater calculations

| Crater | $\bar{X}$ DN (C) | $\bar{X}$ DN (M) | S.D. overlap GT 5? | $\bar{X}$ Mg/Al DN (crater vs mare) | BASALT DEPTHS (m) XRF | Dellon | Horz |
|---|---|---|---|---|---|---|---|
| 1. Anville (Taruntius G) | 129 | 127 | | + 2 | GT 695 | 500-750 | (250-375) |
| 2. Asada (Taruntius A) | 82 | 77 | | + 5 | GT 860 | (0-250) | (0-125) |
| 3. Beer | 83 | 88 | | - 5 | LT 495 | 0-500 | 0-250 |
| 4. Beketov (Jansen C) | 107 | 107 | X | 0 | | 250-500 | 125-250 |
| 5. Bernini (Jansen L) | 118 | 117 | | + 1 | GT 460 | 500-750 | (250-375) |
| 6. Bessel | 121 | 141 | | -20 | LT 530 | no data | no data |
| 7. Bobillier (Bessel E) | 161 | 132 | | +29 | GT 430 | no data | no data |
| 8. Borel (Le Monnier C) | 128 | 112 | | +16 | GT 330 | no data | no data |
| 9. Cauchy | 99 | 118 | | -19 | LT 860 | 250-500 | 125-250 |
| 10. Clerke (Littrow B) | 120 | 111 | X | + 9 | | 0-250 | 0-125 |
| 11. Dawes | 114 | 113 | X | + 1 | | 250-500 | 125-250 |
| 12. Ibn Battuta (Goclenius A) | 70 | 94 | | -24 | LT 400 | (750-1000) | 375-500 |
| 13. Lindbergh (Messier G) | 105 | 105 | | 0 | GT 595 | 500-750 | (250-375) |

$\bar{X}$ DN (C) = mean density number for the crater
$\bar{X}$ DN (M) = " " " " " mare
SD = standard deviation
GT = greater than
LT = less than

Table 2. (cont.)



| Crater | $\bar{X}$ DN (C) | $\bar{X}$ DN (M) | S.D. overlap GT 5? | X Mg/Al DN (crater vs mare) | BASALT DEPTHS (m) XRF | Dellon | Horz |
|---|---|---|---|---|---|---|---|
| 14. Messier and 15. Messier A | 124 | 119 | X | + 5 | | 1000 | 500 |
| 16. Peek | 94 | 97 | | - 3 | LT 760 | 500 | 250 |
| 17. Peirce | 105* | 115 | X | +10 | | no data | no data |
| 18. Picard | 146 | 124 | | +22 | GT 726 | GT 1000 | GT 500 |
| 19. Plinius | 103 | 116 | X | -13 | | LT 250 | LT 125 |
| 20. Ross | 94 | 112 | X | -18 | | 250-500 | 125-250 |
| 21. Secchi K | 105 | 108 | X | - 3 | | 500-750 | 250-375 |
| 22. Sinas | 122 | 122 | X | 0 | | 750-1000 | 375-500 |
| 23. Sinas E | 128 | 124 | X | + 4 | | 500-750 | 250-375 |
| 24. Sulpicious Gallus | 102 | 113 | | -11 | LT 695 | LT 250 | LT 125 |
| 25. Tacquet | 107 | 110 | | - 3 | LT 430 | 0-250 | 0-125 |
| 26. Tacquet C | 132 | 127 | | +12 | GT 595 | (250-500) | (125-250) |
| 27. Taruntius | 84 | 109 | | -25 | LT 400 | 0-250 | 0-125 |
| 28. Taruntius H | 87 | 96 | | - 9 | LT 595 | 500-750 | 250-375 |
| 29. Taruntius P | 100 | 126 | | -26 | LT 460 | 250-500 | 125-250 |
| 30. Timocharis | 95 | 104 | X | - 9 | | 500-750 | 250-375 |
| 31. Unnamed in Smythii | 102 | 109 | X | - 7 | | 250-500 | 125-250 |
| 32. Zahringer (Taruntius E) | 129 | 123 | X | - 1 | | 250-500 | 125-250 |

* continuous ejecta - crater interior not within data coverage
$\bar{X}$ DN (C) = mean density number for the crater
$\bar{X}$ DN (M) = " " " " " mare
SD = standard deviation
GT = greater than
LT = less than